The Journal of Chemical Physics

Quantum-state-resolved studies of aqueous evaporation dynamics: NO ejection from a liquid water microjet

Cite as: J. Chem. Phys. **150**, 044201 (2019); https://doi.org/10.1063/1.5083050
Submitted: 27 November 2018 . Accepted: 02 January 2019 . Published Online: 23 January 2019

Mikhail Ryazanov, and David J. Nesbitt

Quantum-state-resolved studies of aqueous evaporation dynamics: NO ejection from a liquid water microjet

Cite as: J. Chem. Phys. **150**, 044201 (2019); doi: 10.1063/1.5083050
Submitted: 27 November 2018 • Accepted: 2 January 2019 •

Mikhail Ryazanov[1] and **David J. Nesbitt**[1,2,3]

AFFILIATIONS

[1] JILA, National Institute of Standards and Technology and University of Colorado, Boulder, Colorado 80309, USA
[2] Department of Physics, University of Colorado, Boulder, Colorado 80309, USA
[3] Department of Chemistry, University of Colorado, Boulder, Colorado 80309, USA

ABSTRACT

This work presents the first fully quantum-state-resolved measurements of a solute molecule evaporating from the gas–liquid interface in vacuum. Specifically, laser-induced fluorescence detection of NO($^2\Pi_{1/2,\,3/2}$, v = 0, J) evaporating from an ∼5 mM NO–water solution provides a detailed characterization of the rotational and spin–orbit distributions emerging from a ⌀4–5 μm liquid microjet into vacuum. The internal-quantum-state populations are found to be well described by Boltzmann distributions, but corresponding to temperatures substantially *colder* (up to 50 K for rotational and 30 K for spin–orbit) than the water surface. The results therefore raise the intriguing possibility of *non-equilibrium dynamics* in the evaporation of dissolved gases at the vacuum–liquid-water interface. In order to best interpret these data, we use a model for *evaporative cooling* of the liquid microjet and develop a model for *collisional cooling* of the nascent NO evaporant in the expanding water vapor. In particular, the collisional-cooling model illustrates that, despite the $1/r$ drop-off in density near the microjet greatly reducing the probability of collisions in the expanding water vapor, even small inelastic cross sections ($\lesssim$ 20 Å^2) could account for the experimentally observed temperature differences. The current results do not rule out the possibility of non-equilibrium evaporation dynamics, but certainly suggest that correct interpretation of liquid-microjet studies, even under conditions previously considered as "collision-free," may require more careful consideration of residual collisional dynamics.

https://doi.org/10.1063/1.5083050

I. INTRODUCTION

The surface of a liquid represents an unusually complex and challenging environment for investigation with modern chemical-physics methods, though one of considerable relevance to areas such as molecular uptake into atmospheric droplets and gas–liquid solvation dynamics at the marine boundary layer. In particular, collisions at the gas–liquid interface are crucial to any first-principles understanding of diverse chemical pathways from gas adsorption, accommodation, and dissolution into liquids to heterogeneous gas–liquid-phase catalysis and reactive processing of molecular surfactants on atmospheric aerosols.[1–4] Indeed, even closer to home, such collisional processes are fundamental to molecular O_2 adsorption into (and CO_2 expulsion out of) the blood stream through the lung alveoli, which are obviously responsible for proper breathing and survival of the species.[5,6]

The first step in this complex ladder of dynamical activity is through collisional energy transfer at the gas–liquid interface, which can be probed by molecular-beam experiments exploring the exchange of energy between the projectile's translational, rotational, vibrational, and even electronic degrees of freedom with the liquid interface.[7–11] Although still an emerging scientific frontier, this is an area of research which has seen considerable advances in recent decades, marked by development of powerful molecular-beam experiments pioneered by Fenn and co-workers[12] and later exploited by Nathanson, Minton, and others, based on inelastic collisions of supersonic beams with various liquid surfaces, monitored by time-of-flight (TOF) mass spectrometry on the scattered molecular species.[7,11,13,14]

Of particular interest have been prospects of performing chemistry at the gas–liquid interface. The Minton group, in particular, has utilized novel molecular beams explosively heated by CO_2 laser to achieve high-energy projectiles with multiple-electronvolt translational energies, which has permitted many mass-spectroscopic studies of translationally hyperthermal chemical reaction dynamics at gas–liquid and gas–solid interfaces.[10,13,15,16] Perkins and co-workers have taken advantage of molecular beams and discharge sources to inelastically and reactively scatter molecules and radicals from a variety of liquid surfaces, probing quantum-state and translational distributions of the scattered molecules by direct IR-laser absorption and high-resolution Dopplerimetry methods.[17–21] The McKendrick group has elegantly applied quantum-state-resolved techniques with UV photolysis sources of translationally hot OH and $O(^3P)$ colliding with hydrocarbon and room-temperature ionic liquids (RTILs), probing the resulting rovibrational distributions of $OH(v, N)$ by laser-induced fluorescence (LIF).[9,16,22–24] The net result of all these studies has been deeper mechanistic insights into chemical and physical properties of the gas–liquid interface.

One limitation to such methods has been the need for sufficiently low vapor pressure to permit the molecule to impinge on and escape from the liquid interface without suffering collisional scrambling of the nascent quantum-state distributions. This is especially the case for liquid water, which is clearly the most important and yet challenging solvent to study. Simply stated, the high vapor pressure of liquid water (612 Pa = 4.6 Torr at the triple point)[25] prevents studies of gas–surface dynamics by macroscopic probes near a flat liquid interface, since even at the nominal freezing point (273 K), the mean free path λ_0 in the vapor phase above the surface spans only several micrometers. This means that molecules leaving the surface inevitably undergo multiple collisions prior to reaching a detection point any macroscopic distance away from the water interface. Thus, the nascent distributions of the evaporant over spin–orbit, electronic, vibrational, rotational, and translation degrees of freedom are compromised by collisions prior to measurement.

A clever technique to circumvent (or at least significantly reduce) this problem, first proposed by Faubel, Schlemmer, and Toennies,[26] has been to exploit the water surface in the form of a "microjet," that is, a flowing liquid column with a micrometer-scale radius (r_0) on the order of the gas-phase mean free path (λ_0). For such cylindrical geometries, the vapor density drops approximately inversely with the distance from the jet axis. Thus, although the number density in the immediate proximity of the jet is as high as near a flat water surface, it drops to much lower values on the r_0 length scale. In principle, for sufficiently small jet diameters, the average number of collisions in the macroscopic path between the liquid surface and detection regions can be made arbitrarily small. In practice, however, the jet diameter is limited to several micrometers, as the problems with rapid evaporative cooling, jet disintegration, and nozzle clogging tend to grow rapidly with reduction in jet thickness.

Microjets of pure water, water solutions, and moderately viscous liquids such as hydrocarbons[27] have been successfully used in studies where high-vacuum conditions are required. These applications include x-ray[28] and photoelectron[29] spectroscopy of the solutes and liquids themselves, as well as time-of-flight (TOF) studies of the velocity distributions for evaporating atomic and molecular solutes as large as an acetic acid dimer $(CH_3COOH)_2$.[30] Of particular relevance to the present work are the TOF studies by Nathanson and co-workers on expulsion dynamics of noble-gas atoms and small molecules.[27,31]

Surprisingly, rather little attention has been devoted to the internal-quantum-state distribution of molecular evaporants. Studies of bulk liquids have been limited to species with low vapor pressure, such as Na_2 evaporating from molten sodium.[32] Among microjet studies, there has been a pioneering work by Buntine and co-workers using resonance-enhanced multiphoton ionization (REMPI) for detection of benzene evaporating from a water–ethanol mixture,[33] as well as the Ellis group using laser-induced fluorescence (LIF) for detection of aromatic compounds laser-ablated from a microjet.[34] However, due to the dense rotational structure of such large organic molecules, only rotational envelopes of partially overlapping vibrational bands could be observed in these studies. In the later work by Barinkova,[34] attempts were made to observe the smaller and more spectroscopically resolvable OH radical from photodissociation of acetylacetone dissolved in ethanol jets, but without success.

In this work, we present the first quantum-state-resolved studies of molecules, specifically nitric oxide (NO), evaporating from a liquid water microjet, exploiting LIF detection for measurement of individual populations of all spin–orbit, rotational and Λ-doublet states in the ground electronic state $X^2\Pi$ of NO with high detection sensitivity. This work clearly builds on experimental capabilities obtained from previous studies in our laboratory on quantum-state distributions of NO scattering from a variety of low-vapor-pressure liquids,[35–40] but now extended to a much higher-vapor-pressure solvent of paramount importance and interest.

The organization of this article is as follows: Sec. II describes the experimental approach for probing quantum-state distributions of NO evaporating from a liquid-microjet surface. This is followed by presentation/analysis of the NO LIF data in Sec. III A, which reveal a surprising experimental result. Specifically, the emerging NO is observed with rotational and spin–orbit temperatures *significantly colder* (by up to 50 K) than the microjet surface. This behavior is further explored by detailed studies of these NO quantum-state distributions as functions of distance away from and along the microjet (Sec. III B), as well as the initial microjet temperature (Sec. III C).

These observations shape the central focus of this article. Specifically, we consider whether the NO simply evaporates from the water microjet with *a non-equilibrium* *distribution* of internal states, which by detailed balance would have important implications for the quantum-state dependence of impulsive scattering vs trapping-desorption dynamics. In Sec. IV, we show that such non-equilibrium effects are at least *not required* by the data, as demonstrated by exploring two effects that could potentially contribute to lower NO temperatures. In Sec. IV A, we first consider rapid *evaporative cooling* of the liquid water microjet in the first few millimeters of travel through vacuum, from which the ejected NO originates. However, we demonstrate that this effect explains neither the magnitudes nor trends in the observed temperature differences. In Sec. IV B, we then consider whether collisions between NO and the adiabatically expanding water vapor could be sufficient to reduce the internal temperature of NO evaporant. We present an analytic model of collision dynamics in the water vapor surrounding the microjet, which reveals that the experimentally observed NO rotational and spin–orbit temperatures would be consistent with such collisional-cooling effects. Indeed, we find that remarkably good agreement with the experimental data for all liquid-microjet temperatures can be achieved based on quite small effective cross sections ($\sigma_{\text{eff}} \lesssim 20$ Å^2) for inelastic collisional energy transfer between NO and the co-expanding H_2O. This article concludes with Sec. V, which summarizes the potential implications of such collisional-cooling dynamics in the accurate analysis and interpretation of previous liquid water microjet studies and outlines important directions for future exploration.

II. EXPERIMENT

The studies of quantum-state-resolved NO evaporation dynamics from a liquid water microjet are performed in a vacuum chamber (60 cm × 60 cm × 60 cm) pumped with a 1200 l/s turbomolecular pump through a liquid-nitrogen cryogenic baffle. With the flowing microjet in operation, the working pressure in the chamber is $\lesssim 10^{-5}$ mbar, resulting in mean free paths many times larger than the chamber dimensions. We are thus confident that collision probabilities for NO macroscopically far away from the jet can be safely neglected.

The NO solutions are prepared by dissolving NO gas at 2.7 bars (2000 Torr) in degassed high-performance liquid chromatography (HPLC)-grade water in a stainless-steel mixing cylinder, resulting in an ~5 mM solution (~10^{-4} NO mole fraction) and transferred to a syringe pump (Teledyne ISCO 500D) prior to the experiment. The (vertical) liquid microjet is generated by pumping the solution at a high pressure ($\gtrsim$100 bars, ~0.1 ml/min flow rate) through a quartz nozzle drawn from HPLC capillary tubing and mounted in an HPLC filter with 0.5 μm pore size. The filter itself is mounted to an XYZ translational stage such than the nozzle orifice can be precisely positioned with respect to the chamber center.

The filter, besides protecting the nozzle from clogging due to trace particulate contamination in the lines, is used for controlling the initial temperature of the microjet. This is achieved by pumping a coolant through a metal coil soldered to the filter body and monitoring the filter-body temperature (T_f) with ±0.5 °C accuracy by an attached thermocouple. Due to the small internal volume of the HPLC filter and a relatively high flow rate, the solution pumped through the filter does not have sufficient time to completely equilibrate with it in temperature. Thus, conversion from T_f to the initial jet temperature $T_{\text{jet}}{}^0$ is performed by linear interpolation between two reference points: the T_f value at which the microjet is observed to freeze ($T_{\text{jet}}{}^0$ = 273 K) and room temperature, for which $T_{\text{jet}}{}^0$ equals T_f.

The microjet diameter is a crucially important parameter in all analyses presented. Although reasonably precise values (±1 μm) can be obtained by direct measurement with an optical microscope, much more quantitatively reliable measurements (±0.1 μm accuracy) are extracted from the analysis of the transverse diffraction pattern created by scattering a 640 nm diode-laser beam from the cylindrical region of the jet.[41,42]

Since the flow rate through the nozzle is limited by the temperature-dependent solution viscosity, we adjust the backing pressure to keep this flow rate constant at all temperatures. For an ~4 μm nozzle exit diameter, the flow rate at pressures $\gtrsim$100 bars is ~0.1 ml/min, resulting in typical jet speeds of ~100 m/s. Under these conditions, the length of laminar flow (measured with an optical microscope) is $\gtrsim$1 mm (increasing slightly at lower temperatures), after which the jet quickly breaks into a stream of droplets due to Plateau–Rayleigh instabilities.[43] At the bottom of the chamber, this droplet stream is collected in a glass bottle cooled by liquid nitrogen to quench further evaporation. Although NO itself does have appreciable vapor pressure ($\gtrsim$0.07 mbar) even at liquid-nitrogen temperature,[44] the dissolved NO remains locked in the water ice. Thus, accumulation of frozen NO–water solution during the experiment does not affect the background level of NO in the chamber.

The NO molecules escaping from the liquid microjet are state-selectively excited on the $A^2\Sigma(v' = 0, J', \varepsilon') \leftarrow X^2\Pi_{1/2,3/2}(v'' = 0, J'', \varepsilon'')$ band by a pulsed tunable UV laser (frequency-tripled (two Inrad Autotracker III units with BBO crystals) output of a dye laser (Continuum ND6000) pumped with the second harmonic of a Q-switched Nd:YAG laser (Continuum PL8010) operating at 10 Hz repetition rate. The laser tuning rate is 0.2 cm^{-1}/s, resulting in 0.02 cm^{-1} wavenumber steps and yielding ~50 samples per NO spectral line. The laser beam passes horizontally through the center of the chamber with a nearly Gaussian spatial profile of 1.0 mm full width at half-maximum (FWHM).

The resulting $A^2\Sigma(v' = 0) \rightarrow X^2\Pi(v'')$ fluorescence is monitored by a photomultiplier tube (PMT) through an objective (⌀45 mm aperture, 32 mm front focal length) mounted perpendicular to both the jet and the laser-beam axes and focused at the center of the chamber, as shown in Fig. 1. A circular diaphragm installed in the image plane limits the field of view to a ⌀3 mm spot, with the intersection of this field of view with the laser beam defining the LIF detection region. The scattered laser light is blocked by a long-pass color filter (UG5, 240–395 nm bandpass) installed after the diaphragm. Although this filter does block the $A^2\Sigma(v' = 0) \rightarrow X^2\Pi(v'' = 0)$ emission (~226 nm), it transmits photons in

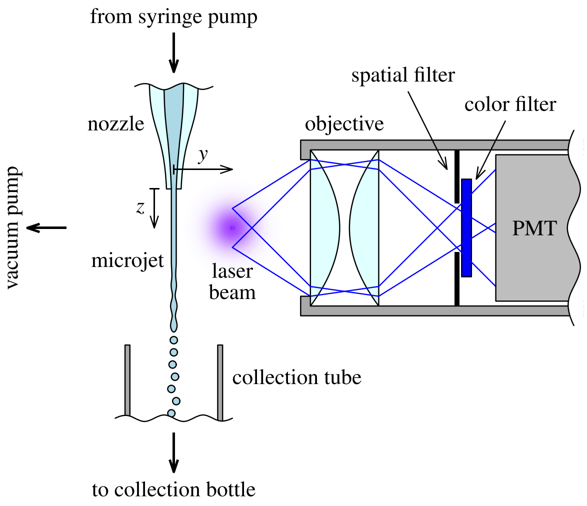

FIG. 1. Schematic drawing of the experimental microjet apparatus, using laser-induced fluorescence (LIF) to probe quantum-state-resolved NO evaporating from the liquid-water surface. The downstream distance *z* is measured vertically from the nozzle exit, with the radial distance *y* measured horizontally from the jet axis toward the LIF detection region.

the other $A^2\Sigma(v' = 0) \rightarrow X^2\Pi(v'' > 0)$ bands carrying most of the fluorescence intensity. Taking into account collection geometry, chromatic aberrations, optics transmission, and NO emission spectra, we estimate the total LIF collection efficiency to be ∼4%. The PMT signals are integrated over a 500 ns temporal window, starting 20 ns after the laser pulse to avoid contamination by residual scattered laser light, and normalized to pulse energy on a shot-to-shot basis. Since the lifetimes of all NO excited states involved are experimentally indistinguishable (193 ± 1 ns),[45] this gating introduces no quantum-state-dependent bias.

All LIF spectra are taken with the laser pulse energy limited to ≲0.5 μJ to ensure excitation in a linear regime even for the strongest transitions. The quantitative reliability of the measurements is tested by analyzing LIF spectra for a static room-temperature NO gas fill (∼10^{-6} mbar, similar to NO levels from the microjet in these experiments, in ∼0.1 mbar N_2 buffer). The populations obtained by fitting the resulting spectrum reproduce the correct room-temperature Boltzmann distribution for both spin–orbit and rotational degrees of freedom within experimental uncertainty. Furthermore, as the cylindrical microjet geometry could in principle result in a non-isotropic distribution of NO $|J, M_J\rangle$ states, we have performed LIF measurements using both vertical and horizontal polarizations. The resulting spectra are also found to be identical within experimental uncertainties, with the results reported herein reflecting the arbitrary choice of vertical laser polarization.

III. RESULTS

A. Analysis of LIF spectra

Figure 2 displays two representative regions of a typical LIF spectrum for NO evaporating from a ⌀4.4 μm liquid microjet. For the strongest lines corresponding to low-J states, the shot-noise-limited signal-to-noise ratio (SNR) is ∼10 and the signal-to-background ratio is ∼400. Lines corresponding to J up to 22.5 (E ≈ 880 cm^{-1}) are readily seen with SNR ∼ 2. Lines up to J ≤ 36.5 (E ≲ 2300 cm^{-1}) are also present in this spectral region, but with correspondingly lower SNR.

Quantum-state populations are extracted from the experimental spectra by a weighted least-squares fitting based on line positions and absorption coefficients from the LIFBASE model.[45] Since most lines in the spectrum are partially overlapped, it is necessary to perform global contour fitting in order to obtain reliable line intensities and state populations. Although Doppler broadening predicts only a ≲0.2 cm^{-1} full width at half-maximum (FWHM), the observed lines exhibit slightly larger widths (FWHM ≈0.4 cm^{-1}) limited primarily by the laser line shape. Best fits of the experimental spectra are obtained with an empirical profile

$$f(x) = \mathcal{N} \exp\left[\left(\frac{\sigma}{\gamma}\right)^2\left(1 - \sqrt{1 + \left(\frac{\gamma x}{\sigma^2}\right)^2}\right)\right], \tag{1}$$

where x is the detuning from line center, $\mathcal{N}$ is a normalization factor, and σ and γ are globally fit parameters for all lines in the spectrum. This empirical profile tends toward a Gaussian $\exp[-x^2/(2\sigma^2)]$ near line center and toward a decaying exponential $\exp(-|x|/\gamma)$ in the wings.

Each $X^2\Pi_{|\Omega|}(J)$ level is actually a Λ-doublet with splittings too small to be resolved in the present experiment. Nevertheless, transitions out of each of the Λ-doubled components can be uniquely associated with well-separated spectral lines; thus, the individual Λ-doublet component populations in fact can be determined from the spectrum. However, in all data reported herein, these two Λ-doublet component populations are found to be statistically indistinguishable, which motivates our treatment of each Λ-doublet simply as a degenerate $X^2\Pi_{|\Omega|}(J)$ state.

Sample Boltzmann plots obtained from fitting the NO evaporant spectrum in Fig. 2 are displayed in Fig. 3. The rotational levels within each spin–orbit manifold are described remarkably well by a Boltzmann distribution (note that the 1500 cm^{-1} range corresponds to 8 kT at $T \approx 250$ K), although at a temperature lower than the jet (see below). In each of the experiments, the rotational distributions follow this simple Boltzmann-like behavior. Moreover, both $^2\Pi_{1/2}$ and $^2\Pi_{3/2}$ spin–orbit manifolds exhibit the same rotational temperatures within experimental uncertainties. The consistency of this behavior throughout the full dataset motivates our reporting the results on both manifolds as a single "rotational temperature" T_{rot}.

Despite complete rotational equilibrium within each of the two spin–orbit manifolds, there is clear evidence for non-equilibrium behavior in the spin–orbit distributions. Specifically, the $^2\Pi_{3/2}$ levels (red symbols in Fig. 3) exhibit *systematically higher* populations than the $^2\Pi_{1/2}$ levels (black symbols) for the same internal energy. This means that the two spin–orbit manifolds are not in thermal equilibrium, which we can characterize by an effective "spin–orbit temperature" T_{SO}.

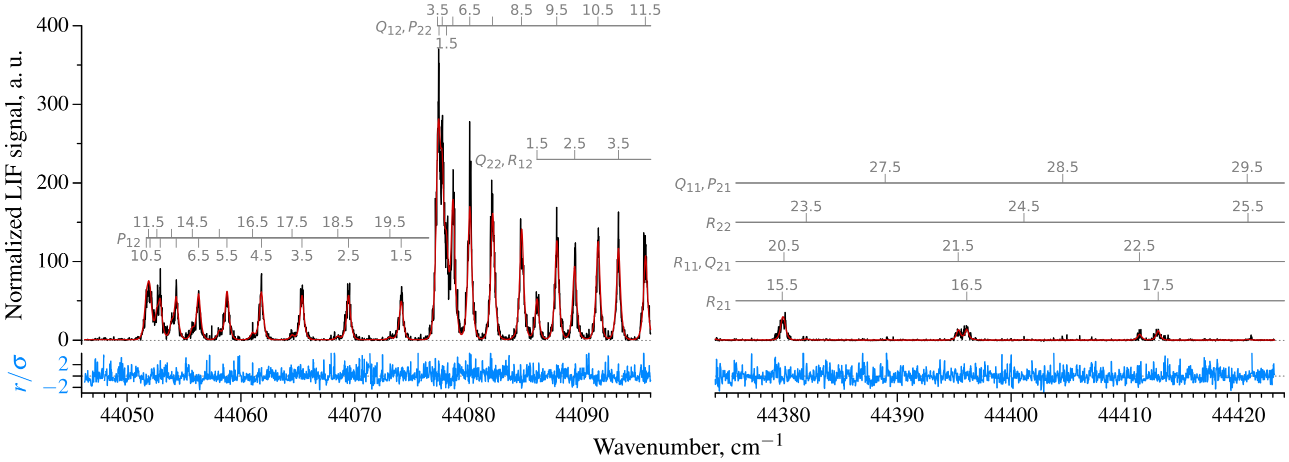

FIG. 2. Two sample LIF spectral regions for NO evaporating from a ⌀4.4 μm water microjet (−4 °C filter temperature, probe laser at $z = 1$ mm, $y = 2$ mm). The region between 44 096 and 44 374 cm^{-1} is removed for clarity. The black line shows the experimental fluorescence intensity normalized to laser pulse energy. The red line indicates the best least-squares fit, with the blue trace below plotting the normalized residuals. Spectral-line assignments with branches and lower-state J'' values are marked with gray lines.

Note that such a 2-state modeling of a spin–orbit temperature cannot be rigorous, since even for a Hund's case (b), the spin–orbit splitting is weakly J-dependent (and the $^2\Pi_{3/2}$ state lacks a J = 1/2 level). To avoid any potential ambiguity, we define T_{SO} such that the predicted relative populations (summed over all J) in the two spin–orbit manifolds match the experimentally observed population ratio

$$\frac{\sum_J (2J+1)\exp\frac{-E(^2\Pi_{3/2},J)}{kT_{SO}}}{\sum_J (2J+1)\exp\frac{-E(^2\Pi_{1/2},J)}{kT_{SO}}} = \frac{\sum_J P(^2\Pi_{3/2},J)}{\sum_J P(^2\Pi_{1/2},J)}. \qquad (2)$$

In summary, this approach simplifies our description of the NO evaporant distributions into two temperatures: one rotational (T_{rot}) from a combined Boltzmann fit to rotational states of both spin–orbit manifolds and one effective spin–orbit (T_{SO}) obtained from the ratio of the two total spin–orbit populations ($[^2\Pi_{1/2}]$ and $[^2\Pi_{3/2}]$) summed over all rotational states. The sum of these two populations also quantitatively characterize the total NO density in the detection region.

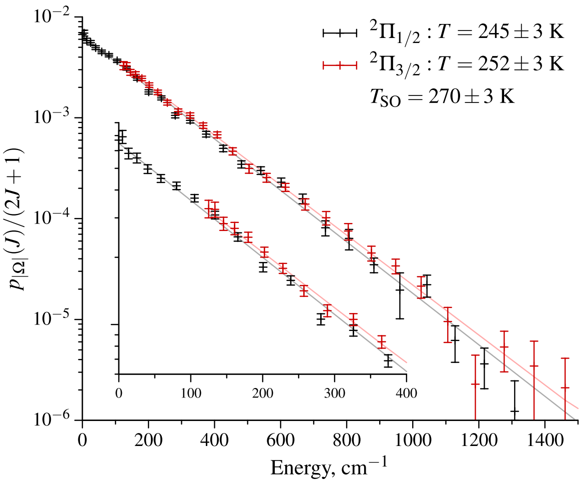

FIG. 3. Boltzmann plots for NO ($^2\Pi_{1/2}$ and $^2\Pi_{3/2}$) showing normalized quantum-state populations ($\sum p = 1$) obtained by fitting the LIF spectrum shown in Fig. 2. State energies are relative to the ground $X^2\Pi_{1/2}$, $J = 1/2$ level. The straight lines represent least-squares fits to a separate Boltzmann distribution for each spin–orbit manifold. The lowest 400 cm^{-1} of the distributions is magnified in the inset to demonstrate the slight but clear differences between the $^2\Pi_{1/2}$ and $^2\Pi_{3/2}$ spin–orbit populations. The corresponding effective spin–orbit temperature is estimated from (2).

B. Axial distance dependences

A liquid microjet in vacuum cools adiabatically due to evaporation,[26,46] resulting in its temperature decreasing with the downstream distance (see Fig. 6) and thus potentially leading to different quantum-state distributions of NO evaporating from different spatial regions of the jet. At the same time, in the absence of any scrambling gas-phase collisions, we would expect the NO internal distributions to be independent of the radial distance from the jet. However, in contrast to time-of-flight experiments, where nascent fluxes are detected only at a particular solid angle, we probe molecules arriving in the detection region from all directions. Thus, measurements at any one downstream distance (z_0) represent a weighted average of molecules evaporating from the entire microjet (both $z < z_0$ and $z > z_0$), although with a predominant contribution from the flux perpendicular to the jet at a similar downstream distance ($z \approx z_0$).

Figure 4 displays the results for a ⌀4.0 μm microjet starting at room temperature (21 °C) and v_{jet} = 86 m/s as a function

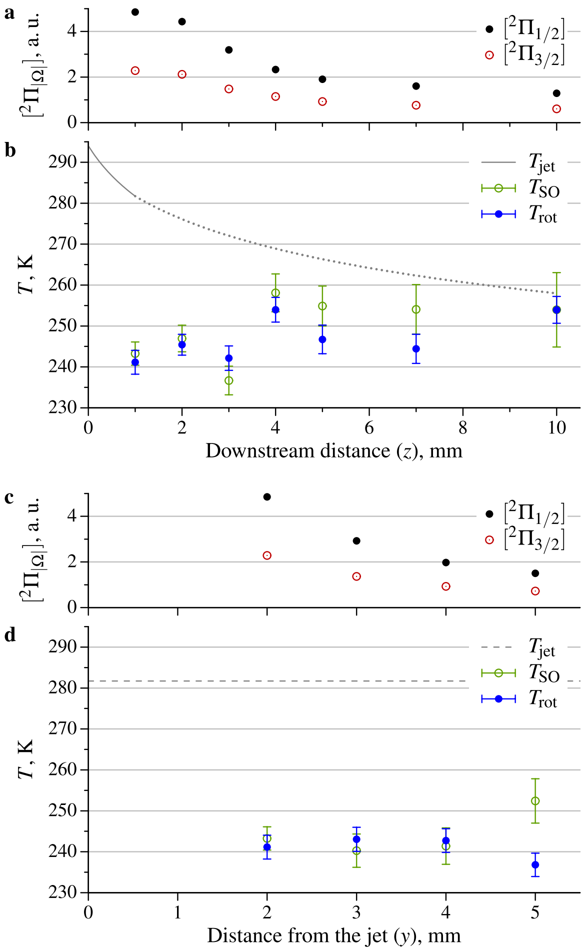

FIG. 4. NO spin–orbit [(a) and (c)] and rotational [(b) and (d)] temperatures measured as functions of downstream (z) and radial (y) distances for a ⌀4.0 μm microjet starting at 294 K. Panels (a) and (b): varying the downstream distance z from the nozzle exit at a constant radial distance $y = 2$ mm from the jet, with the modeled microjet temperature shown for comparison in gray (dotted after jet break-up). Panels (c) and (d): varying the radial distance y at a constant downstream distance $z = 1$ mm from the nozzle exit, with the estimated jet temperature at $z = 1$ mm shown by the dashed gray line.

of downstream (z) and radial (y) distances. The minimal distances are limited to $z = 1$ mm and $y = 2$ mm due to laser-light scatter from the nozzle and the jet, respectively. Figure 4(a) clearly indicates that the NO density drops monotonically with the downstream distance. This behavior is expected and can be attributed to three factors. (1) The equilibrium partial pressure of NO for the solution is 2.7 bars, which is much greater than the water-vapor equilibrium pressure [see Fig. 6(b)]. As a result, the NO initially evaporates from the microjet much faster than water, thus rapidly lowering the NO solute concentration near the surface and decreasing the net NO evaporation rate. (2) Diffusion calculations indicate that on the time scale of the experiment ($\lesssim$100 μs), the NO escape rate is limited by diffusion from the microjet interior to the surface, with a diffusion rate decreasing rapidly with temperature (see Ref. 47 and references therein). Thus as the jet evaporatively cools, NO diffusion to the surface slows, thereby lowering the overall NO escape rate. (3) After the jet breaks into spherical droplets, the surface area per unit length of the stream decreases, which also lowers NO evaporation from the microjet. In contrast to the previous two effects, such a microjet-to-spherical-droplet transition occurs quite abruptly compared to the laminar length. Nevertheless, due to the aforementioned downstream averaging in our LIF detection, this still leads to a relatively smooth NO dependence on the downstream distance, although a sharp intensity drop has been observed in more position-sensitive time-of-flight experiments.[11]

More interesting, however, are the observed rotational and spin-orbit temperatures as functions of the downstream distance [Fig. 4(b)]. Specifically, both T_{rot} and T_{SO} are significantly lower than the jet temperature, especially in the region closest to the nozzle, and even displaying a negative correlation with the microjet temperature, rising as the jet cools downstream. The simple fact that the observed NO is colder than the microjet liquid surface is not unprecedented, as thermal desorption with translational[48] and rotational[37] temperatures lower than the surface temperature has been observed before. However, the *negative* correlation between changes in the gas and the liquid-surface temperatures is surprising and deserves further attention. One possible explanation would be that the escaping NO molecules collide with the co-expanding water vapor, thereby undergoing rotational cooling, much like they would in a supersonic molecular beam. Such cooling effects would obviously be more notable at higher water-vapor densities corresponding to higher microjet temperatures. Thus, the observed trends would at least be qualitatively consistent with post-evaporative cooling of NO by collisions with co-expanding water vapor, a possibility we will explore with analytic modeling of the expansion dynamics in Sec. IV B.

C. Radial distance dependence

The dependences of NO populations and temperatures on the radial distance from the jet at a constant downstream position are summarized in Figs. 4(c) and 4(d). The total NO density [Fig. 4(c)] drops quickly with the distance, with a roll-off between $1/r$ (as expected for a cylindrical source) and $1/r^2$ (as expected for a point source), consistent with a weighted averaging in the LIF detection discussed above. Conversely, the measured NO rotational and spin-orbit temperatures show relatively little dependence on the radial distance over the y = 2–5 mm range, consistent with the collisional cooling occurring mostly close to the microjet surface, where the water vapor density is highest.

It is important to rule out contributions from background NO in the chamber, particularly as we measure progressively weaker NO signals at larger z and y values. To address this issue quantitatively, we have probed NO background contamination by measurements at $y = 10$ mm, $z = -10$ mm, i.e., laterally far away from and even *above* the nozzle exit. This yields total NO densities at least 10-fold lower than at $y = 2$ mm,

z = 1 mm, which provides a safe upper limit of 10% for possible NO background contributions in the important regions close into the microjet. In addition, the rotational and spin–orbit temperatures for NO far from the jet are notably closer to room temperature, consistent with most of the background molecules having thermalized in collisions with the collection tube and/or chamber walls before reaching the detection region. If present, background contamination would therefore appear as a high-energy thermal tail in Boltzmann plots, which is clearly not evident in the data taken close to the microjet (see Fig. 3). In summary, we conclude that effects due to background NO contamination in the chamber can be safely neglected in our analysis.

D. Dependence on initial microjet temperature

In the experiments described above, the dependences on the microjet temperature are inseparable from dependences on geometric parameters, such as temperature and density distributions along the microjet and varying detection geometry. In order to decouple these effects, we have performed an independent set of experiments, varying only the filter temperature T_f, while fixing the detection position at z = 1.0 mm, y = 2.0 mm and the microjet speed at 124 m/s. Specifically, the solution flow thorough a ⌀4.4 μm nozzle is maintained at 113 μl/min by varying backing pressures between 100 and 160 bars (depending on the filter temperature). The reader will notice a slight change in the microjet radius between these studies and the ones described in Secs. II A–II C, unfortunately necessitated by irreversible clogging of such small-diameter nozzles.

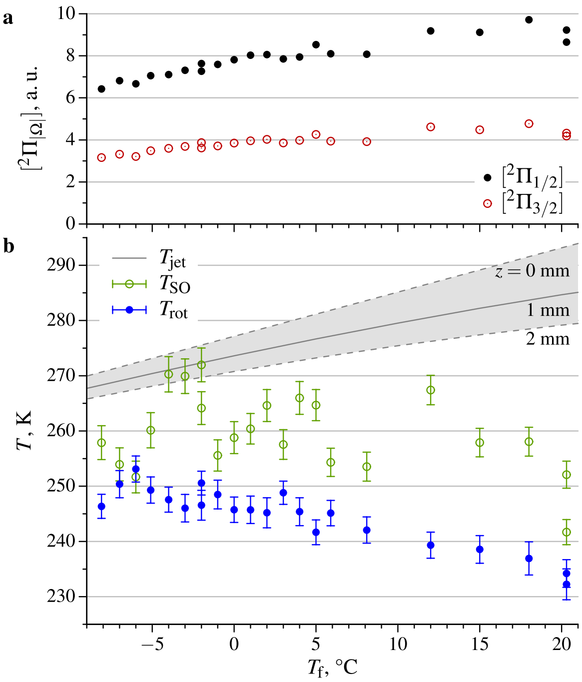

FIG. 5. NO parameters for a ⌀4.4 μm microjet, measured at z = 1 mm, y = 2 mm as functions of the filter temperature T_f. Panel (a): spin–orbit populations (error bars are comparable to symbol size and thus not shown). Panel (b): rotational ($T_{\rm rot}$) and spin–orbit ($T_{\rm SO}$) temperatures. The microjet temperatures predicted from the evaporative-cooling model (see Fig. 6) in the $0 \leq z \leq 2$ mm range are shown for comparison in gray.

These results are summarized in Fig. 5 as functions of filter temperature T_f rather than "microjet temperature" $T_{\rm jet}$ for several reasons. First and foremost, after exiting from the nozzle, the jet starts to cool quickly by evaporation (see Fig. 6), so temperatures in the downstream range contributing to the measured signals change by ∼10 K. Thus, we can at best estimate a characteristic range of $T_{\rm jet}$ influencing the detected NO distributions. Second, T_f is measured directly, but does not directly correspond to the initial jet temperature, as the solution does not have time to achieve complete thermal equilibration with the filter (see Sec. II). Measurements for a range of nozzles operating at similar flow rates indicate that freezing of the microjet solution occurs at $T_f = -5 \pm 2$ °C; however, this might not necessarily correspond to $T_{\rm jet}$ = 273 K (the water triple point) for several competing reasons. One the one hand, the freezing point of water is lowered at high pressures, by 1.2 K at 160 bars, so if the observed microjet freezing is caused by the solution freezing before it reaches the nozzle exit, the resulting microjet might be supercooled by as much as 1.2 K. On the other hand, the solution pumped through the narrow nozzle undergoes frictional heating, which can be estimated from energy conservation

$$p_{\rm back} = \frac{\rho v_{\rm jet}^2}{2} + \rho c_P \Delta T, \tag{3}$$

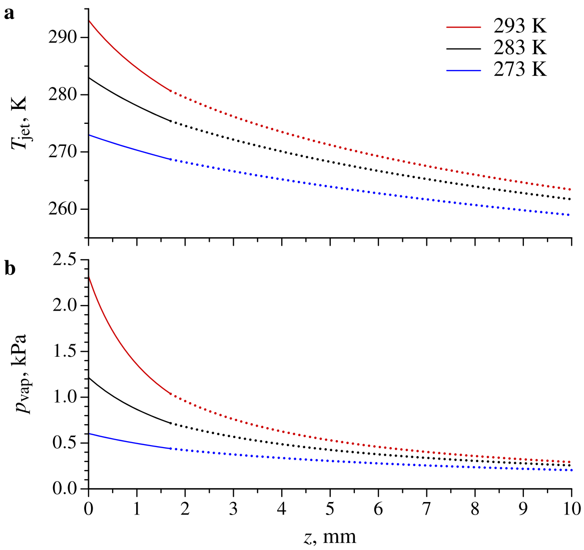

FIG. 6. Panel (a): liquid-water temperature distributions as functions of the downstream position z for a ⌀4.4 μm microjet moving at 124 m/s, calculated for various initial temperatures using the evaporative-cooling model (see Sec. IV A), with dotted lines drawn after the microjet break-up. Panel (b): equilibrium vapor pressure of water at the corresponding $T_{\rm jet}$ values in panel (a).

where p_{back} is the backing pressure, ρ is the water density, and c_P is the water specific heat capacity (both ρ and c_P are only very weak functions of temperature and pressure in the relevant range). This predicts a warming by $\Delta T \approx 2$ K for $p_{\mathrm{back}} = 160$ bars and $v_{\mathrm{jet}} = 124$ m/s. Thus, if freezing occurs before the nozzle exit, the initial jet temperature could be as much as 2 K higher. For all of these reasons, our best estimate is that the initial $T_{\mathrm{jet}} = 273$ K corresponds to $T_f = -5 \pm 2$ °C. Interestingly, the lowest value in Fig. 5 ($T_f = -8$ °C) is slightly below this estimated freezing temperature, meaning that the exiting jet is slightly supercooled. Such supercooling is only observed for new, clean nozzles, but always disappears after a first freeze (if the nozzle is not completely destroyed by freezing!), probably due to the formation of microscopic defects in the nozzle wall that promote rapid nucleation.

One clear trend in Fig. 5(a) is that the total population of NO evaporant decreases systematically with decreasing T_f. Since now all experimental parameters, except the jet temperature, remain unchanged, this effect can be unambiguously attributed to the temperature dependence of the NO diffusion rate. Indeed, the observed ~30% decrease in the total NO population is in excellent agreement with the 32% decrease in the NO diffusion constant[47] from 1.9×10^{-3} $\mu\mathrm{m}^2/\mu\mathrm{s}$ at 285 K to 1.3×10^{-3} $\mu\mathrm{m}^2/\mu\mathrm{s}$ at 268 K.

Of particular interest, the NO rotational temperatures in Fig. 5(b) are again significantly lower than the predicted range of microjet temperatures and clearly exhibit trends in qualitative opposition to it. The difference $T_{\mathrm{jet}} - T_{\mathrm{rot}}$ is as large as ~50 K at $T_{\mathrm{jet}} = 285$ K, and even at $T_{\mathrm{jet}} = 268$ K, slightly below the water freezing temperature, it is $\gtrsim 15$ K. The spin–orbit temperatures exhibit significantly more scatter, but generally follow a similar pattern of being lower than the predicted microjet temperatures, yet higher than the rotational temperatures. Since the only parameter changing in this series of experiments is the jet temperature, the T_{rot} and T_{SO} values can depend only on the liquid-surface temperature directly or indirectly through the water-vapor density.

IV. DISCUSSION

A. Evaporative cooling of the microjet

In order to interpret the observed NO evaporation dynamics, we must first determine the surface temperature of the microjet as a function of distance downstream. Although this could in principle be measured by Raman spectroscopy,[46] we do not currently have this experimental capability and therefore rely on the initial microjet temperature and simulate its evolution by an evaporative-cooling model. Specifically, if we assume a unity sticking coefficient for water molecules at the microjet surface and no recondensation, then the molecular flux of water evaporating from the jet surface is predicted by the Hertz–Knudsen equation

$$\Phi(T) = \frac{\rho_{\mathrm{vap}}(T)}{\sqrt{2\pi MRT}}, \tag{4}$$

where M is the water molar mass and R is the gas constant. The resulting temperature change in the microjet can be calculated from energy conservation

$$c_P(T)\rho(T)\delta V\, dT = -L(T)\Phi(T)\delta S\, dT, \tag{5}$$

where the water molar heat capacity c_P, molar density ρ, molar heat of evaporation L, and equilibrium vapor pressure p_{vap} are known functions of temperature,[49,50] and the comoving volume and surface elements are correspondingly $\delta V = \pi r_{\mathrm{jet}}^2 \delta z$, $\delta S = 2\pi r_{\mathrm{jet}} \delta z$ for the cylindrical jet and $\delta V = \frac{4}{3}\pi r_{\mathrm{d}}^3$, $\delta S = 4\pi r_{\mathrm{d}}^2$ for the spherical droplets after break-up. If we assume that Plateau–Rayleigh instabilities in the microjet are driven by the fastest-growing surface wave ($\lambda \approx 9.01\, r_{\mathrm{jet}}$),[43] we predict the droplet radius to be $r_d \approx 1.891\, r_{\mathrm{jet}}$ at the point of break-up. If we further impose conservation of molecules $\rho d(\delta V) = -\Phi \delta S dt$ and use the relation $dz/dt = v_{\mathrm{jet}}$, we obtain a system of ordinary differential equations, which can be numerically integrated (treating the break-up process as instantaneous) to obtain $T_{\mathrm{jet}} \equiv T(z)$ and the corresponding $p_{\mathrm{vap}}(z)$ profile as functions of the downstream distance. These results are illustrated in Fig. 6 for different initial microjet temperatures. Deviations from this model due to non-unity sticking probabilities at the liquid–vapor interface or partial recondensation of the evaporated water will decrease the net evaporation rate, reducing the cooling rate and thus leading to actual jet temperatures *higher* than predicted. This obviously would not change the key conclusion in Sec. III that the experimentally observed values of T_{rot} and T_{SO} for NO are significantly *below* the predicted microjet temperature.

B. An analytic collisional-cooling model for NO evaporant

The microjet literature has tended to follow the tradition of estimating collisional effects from the "number of collisions" along a straight line from the jet to the detection region, the rough argument being that if this number is $\ll 1$, the effect of collisions can be neglected. Moreover, in many cases, this number has been calculated using a hard-sphere model with a radius taken as the zero crossing or minimum of some model potential. This approach, however, ignores the attractive long-range part of the potential, which is important for strongly dipolar molecules such as water and thus, in particular, can significantly underestimate the collisional cross sections at low collision energies. In order to more reliably interpret the observed differences between the NO evaporant and microjet temperatures, we next develop a *simple analytic* model for collisional cooling of the nascent NO in the much denser stream of co-evaporating H_2O molecules.

To calibrate our intuition, Table I provides a compilation of cross sections relevant to our modeling of NO collisions with water vapor. We are not aware of any experimental or theoretical studies for the NO–H_2O system; hence, data from related systems with either NO or H_2O substituted are listed as proxies. We are interested mostly in the NO–H_2O J-changing cross section (σ_J), as well as the H_2O–H_2O momentum-transfer (σ_{tr}) and J-changing cross sections (σ_J). While σ_{tr} must be smaller than the total collisional cross

TABLE I. Cross sections σ for estimation of H_2O–H_2O and NO–H_2O collisional effects.

System	σ (Å^2)	Type	Conditions	References
H_2O-H_2O	320	Total	920 m/s	54
H_2O-H_2O	140	**J**-changing	353 K	55
HDO-D_2O	380	**J**-changing	353 K	55
O_2–D_2O	305	Total	900 m/s	56
N_2–D_2O	320	Total	900 m/s	56
NO–He	270	Total[a]	500 m/s	57
NO–Ar	310	Total[a]	790 m/s	58

[a] The J-changing cross section from J = 1/2 is about twice smaller.[59,60] See also Ref. 53.

section (σ_{total}), we do not expect it to be as small as ~20–30 Å^2, which has been assumed on occasion in the water-microjet literature.[11,42] σ_J must also be smaller than $\sigma_{\mathbf{J}}$, since collisions can change the vector **J** orientation without changing its magnitude, but as is evident from Table I, in NO($^2\Pi_{1/2}$, J = 1/2) collisions with noble gases, *J*-changing cross sections constitute a large fraction of σ_{total}.

With this as background, we now consider the influence of collisions in the expanding vapor on the observed NO temperature in terms of a simple analytical model, delaying a more detailed discussion about the validity of assumptions till the end. We treat the microjet as an infinite cylinder at constant temperature and invoke that the number density of water vapor drops as

$$n(r) = n_0\frac{r_0}{r}, \quad n_0 = n(r_0) = \frac{1}{2}\frac{\rho_{\text{vap}}(T_0)}{kT_0}, \tag{6}$$

where $r_0 = r_{\text{jet}}$, and n_0 is the vapor density at the jet surface ($T_0 = T_{\text{jet}}$). If we assume the presence of sufficient H_2O-H_2O collisions to maintain a local thermal equilibrium, then the water vapor expands adiabatically with its temperature as a function of distance given by

$$T(r) = T_0\left(\frac{n(r)}{n_0}\right)^{\gamma-1} = T_0\left(\frac{r_0}{r}\right)^{\gamma-1}, \tag{7}$$

where the heat-capacity ratio $\gamma = c_P/c_V$ is 4/3 for water in the temperature range relevant for our experiments.

If we further focus on evaporant molecules reaching the detection region along the radial direction, we can write the probability dP_{coll} of an NO–H_2O collision in the interval dr as $dP_{\text{coll}}(r) = n(r)\sigma\, dr$, where σ is an effective collisional cross section (whose interpretation will be discussed later). Then the probability of NO reaching r_2 from r_1 *without collisions* can be calculated using the Volterra product integral[51]

$$P_{r_2\leftarrow r_1} = \prod_{r_1}^{r_2}\left(1 - dP_{\text{coll}}(r)\right) = e^{-\int_{r_1}^{r_2} n(r)\sigma\, dr}. \tag{8}$$

For the $1/r$ drop-off in water density given by (6), this probability of *not* suffering any collisions between r_1 and r_2 integrates to a simple analytical form

$$P_{r_2\leftarrow r_1} = e^{-\int_{r_1}^{r_2} n_0\frac{r_0}{r}\sigma\, dr} = e^{-n_0\sigma r_0\ln\frac{r_2}{r_1}} = \left(\frac{r_1}{r_2}\right)^{n_0\sigma r_0}. \tag{9}$$

Finally, if we assume that each collision equilibrates T_{NO} with the local water-vapor temperature, the *average* temperature of NO reaching the detection region at r_d can be calculated as

$$\langle T_{\text{NO}}\rangle = \int_{r=r_0}^{r=r_d} T(r)dP_{r_d\leftarrow r} = T_0 P_{r_d\leftarrow r_0} + \int_{r_0}^{r_d} T(r)\frac{P_{r_d\leftarrow r}}{dr}dr, \tag{10}$$

where the probability density for the last collision is

$$\frac{dP_{r_d\leftarrow r}}{dr} = \frac{n_0\sigma r_0}{r}\left(\frac{r}{r_d}\right)^{n_0\sigma r_0}, \tag{11}$$

and the probability $P_{r_d\leftarrow r_0}$ of reaching the detection region from the jet *without collisions* is given by (9). Substitution of (7), (9), and (11) into (10) therefore yields the relatively simple analytical expression

$$\langle T_{\text{NO}}\rangle = T_0\left\{R^{n_0\sigma r_0} + \frac{n_0\sigma(r_d R^\gamma - r_0 R^{n_0\sigma r_0})}{n_0\sigma r_0 - \gamma + 1}\right\}, \tag{12}$$

where $R \equiv r_0/r_d$ is the ratio of the microjet radius to the radius at which NO is detected.

$\langle T_{\text{NO}}\rangle$ values calculated from (12) are plotted in Fig. 7 as a function of T_{jet} for a range of σ values and parameters $r_0 = r_{\text{jet}}$

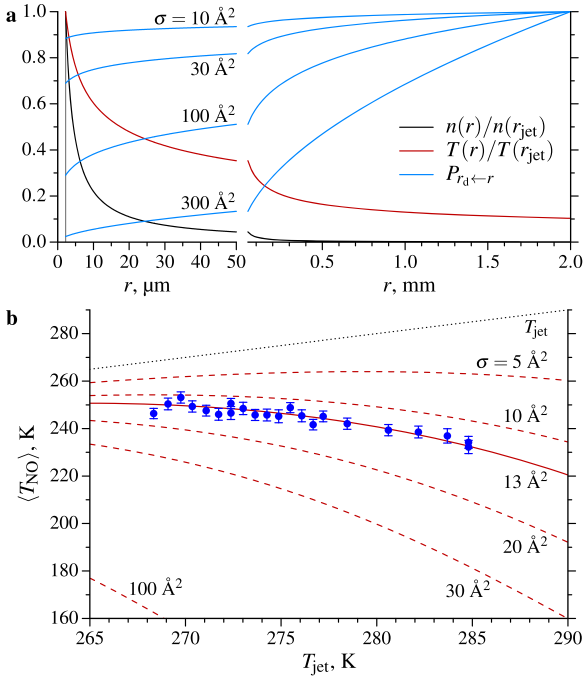

FIG. 7. Model for NO cooling due to collisions in the expanding water vapor. Panel (a): radial profiles for water-vapor density n and temperature T for r_{jet} = 2.2 μm. Also shown is the probability $P_{r_d\leftarrow r}$ for NO molecules to reach the detection region at r_d = 2 mm from radius r *without collisions* for various effective collisional cross sections σ (with T_{jet} = 273 K). Panel (b): resulting NO rotational temperatures calculated using (12) for various effective cross sections. The blue points with error bars represent the experimental T_{rot} values from Fig. 5. Note the remarkable agreement between experimental data and the model with an effective cross section σ = 13 Å^2.

= 2.2 μm, r_d = 2 mm appropriate to the present experimental conditions, together with an illustration of the $n(r)$, $T(r)$, and $P_{r_d \leftarrow r}$ profiles (see also the supplementary material for additional plots). As can be seen in Fig. 7(a), for small σ values, collisions mostly occur close to the microjet and $P_{r_d \leftarrow r} \approx 1$ for $r \gtrsim 1$ mm. Thus, the results become essentially independent of r_d, which is consistent with our experimental data in Fig. 4(d). On the other hand, the observed deviation of $\langle T_{NO} \rangle$ from T_{jet} [see Fig. 7(b)] is predicted to be larger for higher T_{jet}, primarily due to the strong temperature dependence of the initial water-vapor density $n_0(T_{jet})$. However, by far the most striking observation in Fig. 7 is that the experimental results for the $\langle T_{NO} \rangle$ dependence on T_{jet} can be remarkably well matched with an effective collision cross section of only σ = 13 Å^2! The model clearly predicts that rather modest collisional cross sections (on the scale of those in Table I) can lead to appreciable cooling effects.

C. Collision-model assumptions revisited

Returning to a more detailed examination of our model assumptions, we note that σ is an *effective* cross section and differs from the J-changing cross section for several reasons. First, the expression $n\sigma\ dr$ in the collision probability is valid for an NO molecule moving through a swarm of stationary H_2O molecules, whereas in our case, both NO and H_2O are co-moving radially away from the jet. Thus, the collision frequencies will be lower than predicted and decrease as the vapor expands. Second, we assumed that the rotational temperature fully equilibrates with each collision, whereas for J-changing collisions, the probability of changing J by ΔJ drops quickly for $|\Delta J| \gtrsim 1$.[52] Thus, complete equilibration of the rotational distribution requires multiple J-changing collisions. These issues deserve further thought and analysis, but the fact that the effective cross section required in our model is an order of magnitude lower than expected NO–H_2O J-changing cross section is at least not unreasonable.

The assumptions of an infinite jet at a constant temperature and molecules moving only perpendicular to the jet axis appear to be the least justified in the model. As can be seen from Fig. 6, the jet temperature drops noticeably in the region contributing to the measured signal, but more important is that the vapor pressure can exhibit a more than 2-fold drop. This means that the molecules originating from different downstream distances with different initial temperatures and subject to quite different collision probabilities are measured in the experiment. Also, the higher water vapor pressures from the warmer parts of the jet can significantly increase collision probabilities even for the molecules coming from colder parts of the jet, for which a "more collisionless" regime might be expected.

The discussion so far has focused on the NO rotational temperature T_{rot}, but it applies equally well to the effective spin–orbit temperature T_{SO}. As can be seen from Fig. 7(b), T_{SO} lies approximately halfway between T_{jet} and T_{rot}, so the model matches the experimental data with an approximately two-fold smaller effective cross section, although the goodness of this fit is hard to assess due to larger scatter in the T_{SO} data. Such behavior is expected qualitatively, as changing the spin–orbit state in a collision has a lower probability than changing the rotational state. While experimental studies[53] of NO($^2\Pi_{1/2}$, J = 1/2) colliding with Ar reveal SO-changing collisional cross sections smaller than SO-conserving by a factor of ∼4 (with theoretical calculations cited there giving an even larger factor), these experiments have been performed at 55 meV collision energy (roughly two-fold higher than in the present work) and only for $^2\Pi_{1/2}$, J = 1/2 → $^2\Pi_{3/2}$ transitions. In addition, the NO–Ar system might be a poor analog of the NO–H_2O system in terms of spin–orbit branching ratios. However, since a single SO-changing collision could be enough to establish a spin–orbit equilibrium, the corresponding effective cross section in our model might be a closer description than for rotational degrees of freedom.

Finally, it is worth pointing out that an adequately detailed evaporation model must not only include the jet temperature profile but also account for the jet-surface motion. For example, in the present experiments, the jet speed is only ∼4 times lower than characteristic thermal speeds of the NO, which means that the NO molecules in the slower part of the velocity distribution cannot reach the detection region at all. In principle, this should have no effect on the measured NO rotational distributions, unless there is a strong correlation between internal degrees of freedom and escape velocity upon evaporation. However, in TOF measurements, which basically detect only particles with jet-frame $v_z = -v_{jet}$, this should have a noticeable impact on the observed velocity distributions. This effect is less important for lighter species, like H_2O and especially He and H_2, but can be large for heavier evaporates such as Ar (proposed as an intrinsic "thermometer"[31]) and CH_3COOH dimer.[30]

V. CONCLUSION

We have demonstrated first fully quantum-state-resolved measurements for internal-state distributions of molecules evaporating from a liquid microjet, specifically NO dissolved in water. As a key observation, the NO state distributions are found to be well described by rotational and spin–orbit temperatures that are significantly lower (by as much as 50 K) than the liquid surface for the range of temperatures studied (267–285 K). However, a deeper analysis reveals that these observations could be consistent with NO evaporating in thermal equilibrium with the microjet surface, but cooling due to collisions with coexpanding water vapor prior to detection. Our results indicate that a further order-of-magnitude reduction in collision probability will be required to unambiguously probe for non-equilibrium solute-gas expulsion dynamics at the gas–liquid interface. Work with salty water solutions to achieve lower microjet temperatures and thus lower vapor pressures for a reduction in collision probability is currently underway.

Our analysis has broader impacts on microjet studies in general. Specifically, our collisional-cooling model reveals that even a small collision probability can have a noticeable effect on the observed distributions. It is worth noting that in the first microjet studies,[26] the velocity distributions even for a $\varnothing 5$ μm jet at $T_{jet} \approx 245$ K exhibited a radial translation temperature $T_r \approx 140$ K and speed ratio $S \equiv \langle v_r \rangle / \sqrt{2kT_r/m} \approx 1$, i.e., quite far from the expected collisionless Maxwellian distribution. More recent TOF studies[31] have also confirmed that the velocity distribution of water molecules from a $\varnothing 5$ μm jet at $T_{jet} = 252$ K is notably colder than T_{jet}, and even at $T_{jet} = 237$ K, it does not match the expected Maxwellian distribution. Yet another thoughtful example is the study of benzene evaporating from a water–ethanol microjet by Buntine and co-workers,[33] where LIF measurements of the rotational (from band-contour analysis) and vibrational distributions yielded clearly different temperatures, with their analysis of the rotational and vibrational cooling indicating collision probabilities an order of magnitude higher than those given by "traditional" hard-sphere estimates. All these considerations lead us to conclude that even relatively small collision probabilities can exert significant effects on the observed distributions and that the results of previous experiments where collisional effects have been ignored based on an estimate of $N_{coll} \lesssim 1$ will likely require a more careful reinterpretation.

SUPPLEMENTARY MATERIAL

See supplementary material for additional plots of the probability $P_{r \leftarrow r_0}$ of collisionless travel from the microjet to a given radial distance and of the "average number of collisions" calculated within the same model assumptions for comparison with previous studies.

ACKNOWLEDGMENTS

This work was supported in part by the Air Force Office of Scientific Research (Grant No. FA9550-15-1-0090), with additional funds for lasers and construction of apparatus provided by the National Science Foundation (Grant Nos. CHE 1266416, CHE 1665271, and PHY 1734006).

REFERENCES

[1] P. Davidovits, C. E. Kolb, L. R. Williams, J. T. Jayne, and D. R. Worsnop, Chem. Rev. **106**(4), 1323 (2006).

[2] B. J. Gertner and J. T. Hynes, Science **271**(5255), 1563 (1996).

[3] J. P. D. Abbatt, Chem. Rev. **103**(12), 4783 (2003).

[4] G. B. Ellison, A. F. Tuck, and V. Vaida, J. Geophys. Res.: Atmos. **104**(D9), 11633, https://doi.org/10.1029/1999jd900073 (1999).

[5] E. M. Scarpelli, Anat. Rec. **251**(4), 491 (1998).

[6] T. R. Sosnowski, P. Kubski, and K. Wojciechowski, Colloids Surf., A **519**, 27 (2017).

[7] M. E. King, M. E. Saecker, and G. M. Nathanson, J. Chem. Phys. **101**(3), 2539 (1994).

[8] M. E. Saecker, S. T. Govoni, D. V. Kowalski, M. E. King, and G. M. Nathanson, Science **252**(5011), 1421 (1991).

[9] S. P. K. Kohler, M. Allan, H. Kelso, D. A. Henderson, and K. G. McKendrick, J. Chem. Phys. **122**(2), 024712 (2005).

[10] B. H. Wu, J. M. Zhang, T. K. Minton, K. G. McKendrick, J. M. Slattery, S. Yockel, and G. C. Schatz, J. Phys. Chem. C **114**(9), 4015 (2010).

[11] J. A. Faust and G. M. Nathanson, Chem. Soc. Rev. **45**, 3609 (2016).

[12] S. L. Lednovich and J. B. Fenn, AIChE J. **23**(4), 454 (1977).

[13] M. E. King, G. M. Nathanson, M. A. Hanninglee, and T. K. Minton, Phys. Rev. Lett. **70**(7), 1026 (1993).

[14] G. M. Nathanson, P. Davidovits, D. R. Worsnop, and C. E. Kolb, J. Phys. Chem. **100**(31), 13007 (1996).

[15] M. E. King, K. M. Fiehrer, G. M. Nathanson, and T. K. Minton, J. Phys. Chem. A **101**(36), 6556 (1997).

[16] M. A. Tesa-Serrate, E. J. Smoll, T. K. Minton, and K. G. McKendrick, Annu. Rev. Phys. Chem. **67**, 515 (2016).

[17] B. G. Perkins, T. Haber, and D. J. Nesbitt, J. Phys. Chem. B **109**(34), 16396 (2005).

[18] B. G. Perkins and D. J. Nesbitt, J. Phys. Chem. B **110**(34), 17126 (2006).

[19] B. G. Perkins and D. J. Nesbitt, Proc. Natl. Acad. Sci. U. S. A. **105**(35), 12684 (2008).

[20] A. M. Zolot, P. J. Dagdigian, and D. J. Nesbitt, J. Chem. Phys. **129**(19), 194705 (2008).

[21] B. G. Perkins and D. J. Nesbitt, J. Phys. Chem. A **112**(39), 9324 (2008).

[22] M. A. Tesa-Serrate, K. L. King, G. Paterson, M. L. Costen, and K. G. McKendrick, Phys. Chem. Chem. Phys. **16**(1), 173 (2014).

[23] M. Allan, P. A. J. Bagot, S. P. K. Kohler, S. K. Reed, R. E. Westacott, M. L. Costen, and K. G. McKendrick, Phys. Scr. **76**(3), C42 (2007).

[24] P. A. J. Bagot, C. Waring, M. L. Costen, and K. G. McKendrick, J. Phys. Chem. C **112**(29), 10868 (2008).

[25] R. C. Weast, *Handbook of Chemistry and Physics*, 52nd ed. (The Chemical Rubber Company, 1972).

[26] M. Faubel, S. Schlemmer, and J. P. Toennies, Z. Phys. D: At., Mol. Clusters **10**(2), 269 (1988).

[27] D. K. Lancaster, A. M. Johnson, K. Kappes, and G. M. Nathanson, J. Phys. Chem. C **119**(26), 14613 (2015).

[28] K. R. Wilson, B. S. Rude, T. Catalano, R. D. Schaller, J. G. Tobin, D. T. Co, and R. J. Saykally, J. Phys. Chem. B **105**(17), 3346 (2001).

[29] H. L. Williams, B. A. Erickson, and D. M. Neumark, J. Chem. Phys. **148**(19), 194303 (2018).

[30] M. Faubel and T. Kisters, Nature **339**, 527 (1989).

[31] C. Hahn, Z. R. Kann, J. A. Faust, J. L. Skinner, and G. M. Nathanson, J. Chem. Phys. **144**(4), 044707 (2016).

[32] G. Miksch and H. G. Weber, Chem. Phys. Lett. **87**(6), 544 (1982).

[33] O. J. Maselli, J. R. Gascooke, W. D. Lawrance, and M. A. Buntine, J. Phys. Chem. C **113**(2), 637 (2009).

[34] V. Barinkova, "Photoejection of molecules from the surface of a liquid microjet," Ph.D. thesis (University of Leicester, 2009).

[35] M. P. Ziemkiewicz, J. R. Roscioli, and D. J. Nesbitt, J. Chem. Phys. **134**(23), 234703 (2011).

[36] M. P. Ziemkiewicz, A. Zutz, and D. J. Nesbitt, J. Phys. Chem. C **116**(27), 14284 (2012).

[37] A. Zutz and D. J. Nesbitt, J. Phys. Chem. C **119**(16), 8596 (2015).

[38] A. Zutz and D. J. Nesbitt, AIP Adv. **6**(10), 105207 (2016).

[39] A. Zutz and D. J. Nesbitt, J. Chem. Phys. **147**(5), 054704 (2017).

[40] A. Zutz and D. J. Nesbitt, J. Phys. Chem. C **122**(30), 17161 (2018).

[41] C. F. Bohren and D. R. Huffman, *Absorption and Scattering of Light by Small Particles* (Wiley, 1983).

[42] C. D. Cappa, W. S. Drisdell, J. D. Smith, R. J. Saykally, and R. C. Cohen, J. Phys. Chem. B **109**(51), 24391 (2005).

[43] L. Rayleigh, Proc. London Math. Soc. **s1-10**(1), 4 (1878).

[44] E. E. Hughes, J. Chem. Phys. **35**(4), 1531 (1961).

[45] J. Luque and D. R. Crosley, Report No. MP 99-009, 1999.

[46] K. R. Wilson, B. S. Rude, J. Smith, C. Cappa, D. T. Co, R. D. Schaller, M. Larsson, T. Catalano, and R. J. Saykally, Rev. Sci. Instrum. **75**(3), 725 (2004).

[47] S. Pokharel, N. Pantha, and N. P. Adhikari, Int. J. Mod. Phys. B **30**(27), 1650205 (2016).

[48] D. K. Lancaster, *Inert Gas Scattering and Evaporation from Jet Fuel Surrogates Using Liquid Microjets* (University of Wisconsin, 2014).

[49] D. E. Hare and C. M. Sorensen, J. Chem. Phys. **87**(8), 4840 (1987).

[50] D. M. Murphy and T. Koop, Quart. J. Roy. Meteorlog. Soc. **131**(608), 1539 (2005).

[51] A. Slavík, *Product Integration. Its History and Applications* (Matfyzpress, Praha, 2007).

[52] M. Islam, I. W. M. Smith, and M. H. Alexander, Phys. Chem. Chem. Phys. **2**, 473 (2000).

[53] H. Joswig, P. Andresen, and R. Schinke, J. Chem. Phys. **85**(4), 1904 (1986).

[54] W. R. Snow, J. T. Dowell, J. G. Chevrenak, and H. E. Berek, J. Chem. Phys. **58**(6), 2517 (1973).

[55] D. Mammoli, E. Canet, R. Buratto, P. Miéville, L. Helm, and G. Bodenhausen, Sci. Rep. **6**, 38492 (2016).

[56] D. Cappelletti, P. Candori, L. F. Roncaratti, and F. Pirani, Mol. Phys. **108**(17), 2179 (2010).

[57] H. P. Butz, R. Feltgen, H. Pauly, and H. Vehmeyer, Z. Phys. A: Hadrons Nucl. **247**(1), 70 (1971).

[58] H. H. W. Thuis, S. Stolte, J. Reuss, J. J. H. V. D. Biesen, and C. J. N. V. D. Meijdenberg, Chem. Phys. **52**(1), 211 (1980).

[59] M. Yang and M. H. Alexander, J. Chem. Phys. **103**(16), 6973 (1995).

[60] M. H. Alexander, J. Chem. Phys. **99**(10), 7725 (1993).